

## Article

# Controls on Organic Matter Accumulation from an Upper Slope Section on the Early Cambrian Yangtze Platform, South China

Gongjing Zhang <sup>1,2,3,4,\*</sup>, Daizhao Chen <sup>2,3,4</sup>, Yi Ding <sup>5</sup> and Taiyu Huang <sup>6</sup>

<sup>1</sup> Shanxi Key Laboratory of Coal and Coal-Measure Gas Geology, Department of Earth Science and Engineering, Taiyuan University of Technology, Taiyuan 030024, China

<sup>2</sup> Key Laboratory of Cenozoic Geology and Environment, Institute of Geology and Geophysics, Chinese Academy of Sciences, Beijing 100029, China

<sup>3</sup> Innovation Academy for Earth Science, Chinese Academy of Sciences, Beijing 100029, China

<sup>4</sup> University of Chinese Academy of Sciences, Beijing 100049, China

<sup>5</sup> State Key Laboratory of Oil and Gas Reservoir Geology and Exploitation, Chengdu University of Technology, Chengdu 610059, China

<sup>6</sup> General Prospecting Institute, China National Administration of Coal Geology, Beijing 100039, China

\* Correspondence: gjzhang541@163.com

**Abstract:** The early Cambrian witnessed profound environmental changes and biological evolution in Earth's history. During this period, organic-rich shales were widely distributed over almost the entire Yangtze Block. However, the dominant factor that drove the significant accumulation of organic matter (OM) remains controversial and is still debated. Here, we analyzed TOC, organic carbon isotopes, iron speciation, major and trace elements for the lower Cambrian Niutitang Formation in the upper slope Meiziwan section, to investigate the dominant factor controlling OM accumulation. High contents of TOC and Ba<sub>xS</sub> reveal an OM-enriched feature of the Niutitang Formation, and the coupled relationship between them suggest a strong production control on OM accumulation at Meiziwan. Meanwhile, negative relationships between TOC and chemical index of alteration (CIA) values as well as Al contents suggest that influence of chemical weathering and terrestrial input on OM accumulation were limited. Fairly low Co<sub>EF</sub> × Mn<sub>EF</sub> values provide strong evidence that the deposition of organic-rich shales was under the control of oceanic upwelling event. The upwelling event would bring nutrient-rich deep waters into surface water, stimulating phytoplankton bloom and primary productivity in surface water and facilitating OM enrichment. Meanwhile, enhanced accumulation of OM would have promoted subsequent bacterial sulfate reduction, leading to the occurrence of occasional euxinia (evidenced by iron speciation and redox-sensitive trace element data) and promoting preservation of OM. Taken together, our results shed light on the critical role of oceanic upwelling on the marine primary productivity on the earliest Cambrian Yangtze Platform.

**Keywords:** early Cambrian; South China; Niutitang formation; black shales; organic matter accumulation; upwelling event



**Citation:** Zhang, G.; Chen, D.; Ding, Y.; Huang, T. Controls on Organic Matter Accumulation from an Upper Slope Section on the Early Cambrian Yangtze Platform, South China. *Minerals* **2023**, *13*, 260. <https://doi.org/10.3390/min13020260>

Academic Editor: Leszek Marynowski

Received: 2 January 2023

Revised: 10 February 2023

Accepted: 11 February 2023

Published: 12 February 2023



**Copyright:** © 2023 by the authors. Licensee MDPI, Basel, Switzerland. This article is an open access article distributed under the terms and conditions of the Creative Commons Attribution (CC BY) license (<https://creativecommons.org/licenses/by/4.0/>).

## 1. Introduction

The early Cambrian was a critical time interval in Earth's history, witnessing significant tectonic, climatic and biological evolutions [1–3]. During the early Cambrian, organic-matter-enriched shales were widely deposited on a global scale [4,5]. The formation of these important hydrocarbon source rocks was a complicated process, influenced by multiple geological factors, such as primary productivity, redox conditions, and clastic dilution [6–9]. The productivity model supports that primary productivity of surface water is the dominant factor controlling the accumulation of organic matter [7,10,11], which is well illustrated by coastal upwelling zones (e.g., Gulf of California; modern Arabian Sea) [12,13]. Conversely, the preservation model insists that water column anoxia acts as the dominant driver in organic matter accumulation [14,15], and environments such as

restricted basins (e.g., modern Black Sea) provide ideal examples for this model [16]. In addition, the dilution effect of terrestrial siliciclastics could also exert remarkable influence on organic matter accumulation [9,17].

Organic-rich black shales were widely accumulated on the early Cambrian Yangtze Platform (i.e., the Niutitang Formation and its equivalents), providing us a unique window to assess the influence of different factors exerted on organic matter accumulation [5]. Although many studies have focused on the Niutitang Formation black shales during the last decades, the driving force determining the organic matter accumulation is not agreed upon, and the enrichment mechanism of organic matter has been attributed to various factors including (1) high primary productivity [18–21]; (2) intensified oceanic upwelling [18,21–23]; (3) hydrothermal activities [20,24–26]; (4) anoxic sedimentary conditions [18,27]; (5) restricted conditions of the Nanhua Basin during the early Cambrian [27].

In this study, we selected an upper slope section on the early Cambrian Yangtze Platform (i.e., Meiziwan section), using multiple geochemical proxies to investigate ocean redox conditions, primary productivity, upwelling event and chemical weathering of the lower Cambrian organic-rich black shales (i.e., Niutitang Formation). Our primary goal was to distinguish the dominant factor controlling the organic matter accumulation on the early Cambrian Yangtze Platform.

## 2. Geological Setting

### 2.1. Paleogeography and Stratigraphy

The South China Block is composed of the Yangtze Block in the northwest and the Cathaysia Block in the southeast (Figure 1A). These two blocks were sutured together as a united block during the early Neoproterozoic [28]. Subsequently, intensified rifting from ca. 850 to ca. 820 Ma separated the Yangtze and Cathaysia blocks again and led to the development of Nanhua rift basin [29]. During the Ediacaran–Cambrian (E–C) transition, the Yangtze Block underwent block-tilting and intense extensional activity [30,31], leading to the subsequent precipitation of carbonate on paleohighs and cherts/black shales in deeper slope and basin settings [30,32,33].

The studied Meiziwan section is located in Meitan County, Guizhou Province, South China (N: 27°27′22″; E: 107°26′29″). Paleogeographically, it was suggested to be located on the upper slope region of the upper Yangtze Platform (Figure 1B) based on the slump structure and dolobreccias in the Dengying Formation [34,35]. The overlying Niutitang Formation is composed of organic-rich black shales, 13 m of which is exposed at this location. The age at the base of the Niutitang Formation is estimated to be Cambrian Stage 2, based on carbon isotope chemostratigraphy [33,36] and a series of SIMS U–Pb zircon ages [36–39].

### 2.2. Stratigraphic Correlation

Previous studies have conducted a detailed stratigraphic subdivision and correlation of the adjacent Jinsha section and others (ca. 110 km west of Meiziwan section) [23,41,42]. Owing to the incomplete exposure of the Niutitang Formation at Meiziwan, the stratigraphic correlation of the Meiziwan, Jinsha, and Yuanjia sections was conducted using previous data. Carbon isotopic chemostratigraphy has been proven as a reliable proxy for regional and global stratigraphic correlation, especially in the fossil-poor deep water E–C successions [36,41,43–46]. Because the Niutitang Formation is carbonate-poor at the Meiziwan section, only organic carbon isotopic compositions ( $\delta^{13}\text{C}_{\text{org}}$ ) could be obtained and are thus exclusively applied to define its stratigraphic correlation with Jinsha and Yuanjia sections (Figure 2). In this study,  $\delta^{13}\text{C}_{\text{org}}$  and TOC are positively correlated generally (Figure 3), indicating that the variations of  $\delta^{13}\text{C}_{\text{org}}$  are not affected by thermal alteration during diagenesis; if so, a negative correlation between them would be observed since light carbon ( $^{12}\text{C}$ ) is more easily lost and heavy carbon ( $^{13}\text{C}$ ) is gradually enriched due to thermal degradation during diagenesis [47,48]. Hence,  $\delta^{13}\text{C}_{\text{org}}$  data in this study represent near-primary signals of carbon isotope variations of the Niutitang period. Based on the generally increasing trend of the  $\delta^{13}\text{C}_{\text{org}}$  upsection, the Niutitang Formation at Meiziwan

can be correlated to the lower member of the Niutitang Formation at Jinsha and Yuanjia (Figure 2) [41]. The covered interval is assumed to be equivalent to the phosphoritic shale of the basal Niutitang Formation.

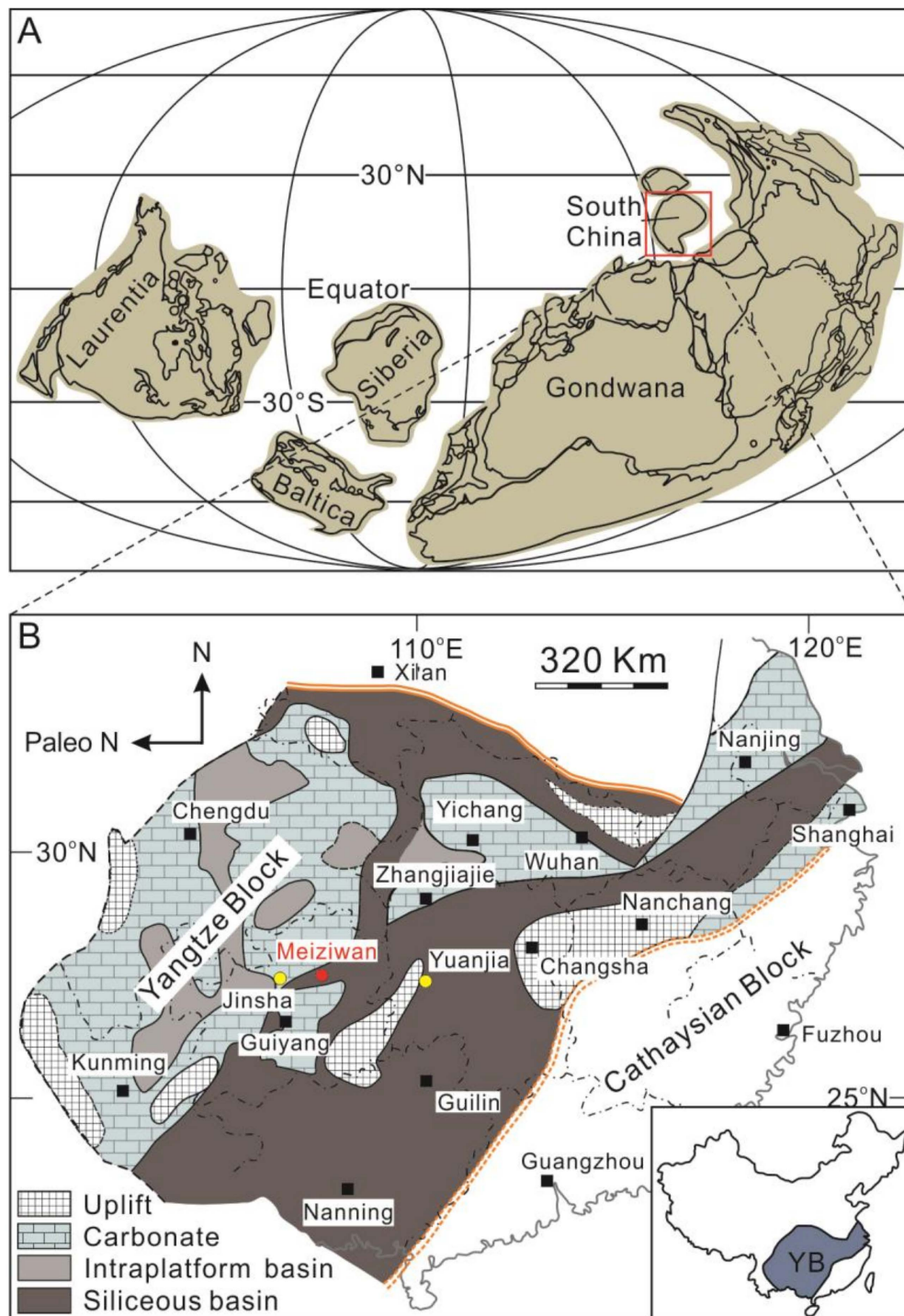


**Figure 1.** (A) Paleolocation of South China Block during the early Cambrian (modified from McKerrow et al. [40]); (B) Paleogeographic map of the Yangtze Block, South China, during the Ediacaran–Cambrian transition (modified from Yeasmin et al. [21]).

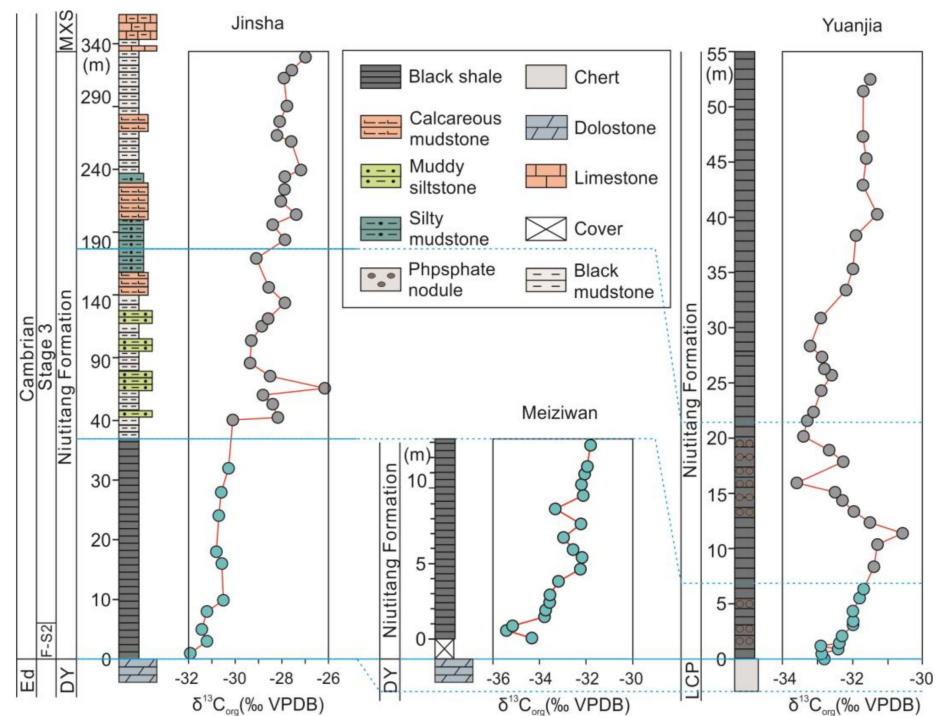


**Figure 2.** Stratigraphic correlation of the Meiziwan with Jinsha and Yuanjia sections based on the variations of  $\delta^{13}C_{org}$ . Data sources: Meiziwan (this study); Jinsha [41]; Yuanjia [49]. Abbreviations: Ed = Ediacaran; F = Fortunian; S2 = Stage 2; DY = Dengying Formation; LCP = Liuchapo Formation; MXS = Mingxinsi Formation. Dashed line refers to uncertainty over the precise correlation position.

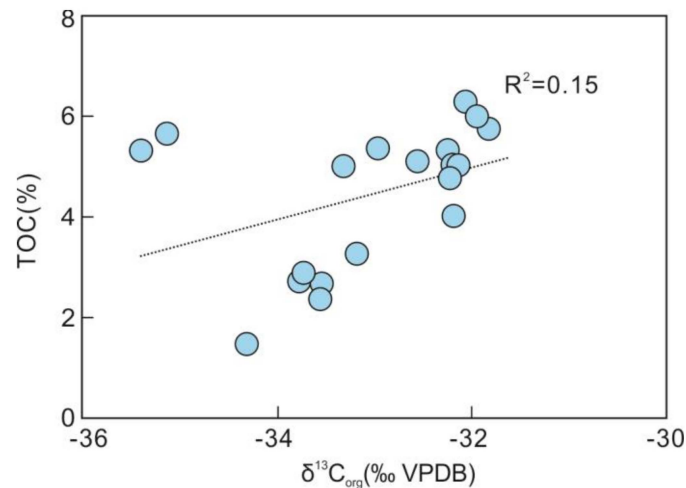


**Figure 3.** Crossplot of  $\delta^{13}C_{org}$  and TOC contents for the Meiziwan section.

### 3. Materials and Methods

A total of 19 fresh samples were collected for geochemical analyses from the Meiziwan outcrop. Firstly, the samples were trimmed in order to remove weathered surfaces, post-depositional veins and pyrite nodules, and then smashed into small pieces. Secondly, the freshest pieces were selected and crushed to <200 mesh powders using a vibratory disc mill (Ti100). Trace elements were analyzed at China University of Geosciences (Beijing), while major elements, TOC and iron speciation were analyzed at the Institute of Geology and Geophysics, Chinese Academy of Sciences (IGGCAS).

Trace element concentrations were analyzed following the steps presented in previous work [50]. Briefly, about 40 mg of sample powders were subjected to successive acid

dissolution and drying, using (1) 0.5 mL concentrated HNO<sub>3</sub> and 0.5 mL concentrated HF; (2) 1 mL HNO<sub>3</sub> and 1 mL HF; (3) 1 mL HNO<sub>3</sub>; (4) 2 mL HNO<sub>3</sub> and 1 mL Milli-Q water (18 MΩ). Then, samples were diluted 2000 folds using Milli-Q water (18 MΩ) before element analyses. Samples were analyzed by inductively coupled plasma–mass spectrometry (ICP-MS) using an Agilent 7500a and the analytical accuracy was better than 5%. The rock standards AGV-2, GSR-1 and GSR-3 were used to monitor the analytical accuracy and precision. Enrichment factors (EFs) for trace elements were expressed as follows:  $X_{EF} = (X/Al)_{\text{sample}} / (X/Al)_{\text{PAAS}}$ , where X represents the targeted element (e.g., Mo, U), and PAAS represents the post-Archean Australian shale [51].

For TOC and isotopic composition of organic carbon ( $\delta^{13}\text{C}_{\text{org}}$ ) analyses, about 200 mg aliquots were acidified using 6 N HCl for 24 h to remove inorganic carbon thoroughly, then neutralized with Milli-Q (18 MΩ) water until pH ~7.0. Then, the samples were dried overnight at 50–60 °C. A EURO EA3000 elemental analyzer and Thermo MAT-253 mass spectrometer were used for TOC and  $\delta^{13}\text{C}_{\text{org}}$  analyses, respectively. Calibration of  $\delta^{13}\text{C}_{\text{org}}$  values was conducted using lab standards USGS24 ( $\delta^{13}\text{C}_{\text{VPDB}} = -16.05\text{‰}$ ) and UREA ( $\delta^{13}\text{C}_{\text{VPDB}} = -49.1\text{‰}$ ). Analytical precision were better than  $\pm 0.5\text{‰}$  and  $\pm 0.2\text{‰}$  for TOC and  $\delta^{13}\text{C}_{\text{org}}$ , respectively.

Iron in carbonate ( $\text{Fe}_{\text{carb}}$ ), oxides ( $\text{Fe}_{\text{ox}}$ ), and magnetite ( $\text{Fe}_{\text{mag}}$ ) were extracted sequentially following the steps presented in previous work [52]. The steps are as follows: (1) ~100 mg sample powder was extracted using sodium acetate solution for  $\text{Fe}_{\text{carb}}$  (50 °C water bath for 48 h with shaking); (2) the sample residue was further extracted using a 50 g/L sodium dithionite solution for  $\text{Fe}_{\text{ox}}$  (50 °C water bath for 2 h with shaking) (3) the sample residue was then extracted using a 0.2 M ammonium oxalate and 0.17 M oxalic acid solution for  $\text{Fe}_{\text{mag}}$  (50 °C water bath for 6 h with shaking). Atomic absorption spectroscope (AAS) was used to analyze the concentrations of Fe of all extracts, and replicate extractions gave a relative standard deviation (RSD) of <5% for all steps. Iron in pyrite ( $\text{Fe}_{\text{py}}$ ) was extracted following the Cr-reduction method [53] and calculated according to the stoichiometric ratio of S: Fe in pyrite. For the analysis, ~1 to 5 g of sample was treated under N<sub>2</sub> and added 20 mL 12 N HCl and 40 mL 1 M CrCl<sub>2</sub> solution and heated for 2 h. The reaction product (H<sub>2</sub>S) was trapped using 20 mL 3% silver nitrate to form Ag<sub>2</sub>S precipitates, which was then filtered, dried, and weighted. The highly reactive iron ( $\text{Fe}_{\text{HR}}$ ) is composed of  $\text{Fe}_{\text{carb}}$ ,  $\text{Fe}_{\text{ox}}$ ,  $\text{Fe}_{\text{mag}}$ , and  $\text{Fe}_{\text{py}}$  [52]. Total Fe is expressed as  $\text{Fe}_{\text{T}}$ .

Major element concentrations were analyzed using X-ray fluorescence spectrometry (XRF). The steps are as follows: (1) 500 mg sample powder was oxidized at 1000 °C lasting 1 h in order to determine the loss on ignition (LOI); (2) oxidized sample powder was mixed with 5000 mg lithium borate; (3) the mixtures were then melted at 1200 °C to make fused glass disks. An AXIOS Minerals (PANalytical) spectrometer was used for analyses, with precision and accuracy better than 5%. Excess Barium ( $\text{Ba}_{\text{xs}}$ ) is assumed to be equivalent to biogenic Ba and calculated as follows:  $\text{Ba}_{\text{xs}} = \text{Ba}_{\text{sample}} - \text{Al}_{\text{sample}} \times (\text{Ba}/\text{Al})_{\text{detr}}$  [17], where  $(\text{Ba}/\text{Al})_{\text{detr}}$  represents the ratio of detrital Ba to Al for the PAAS.

The chemical index of alteration (CIA) is calculated as follows:  $\text{CIA} = \text{molar} [(Al_2O_3)/(Al_2O_3 + CaO^* + Na_2O + K_2O)] \times 100$ , where  $\text{CaO}^*$  equals CaO content in silicate fraction of the sample [54]. CaO can be corrected using the content of P<sub>2</sub>O<sub>5</sub>:  $\text{CaO}^* = \text{mole CaO} - \text{mole P}_2\text{O}_5 \times 10/3$ . If  $\text{CaO}^* > \text{Na}_2\text{O}$ ,  $\text{CaO}^*$  is assumed to be equivalent to Na<sub>2</sub>O, if  $\text{CaO}^* < \text{Na}_2\text{O}$ ,  $\text{CaO}^*$  is used for calculation of CIA [55]. Influence of diagenetic K-metasomatism of source rocks can be corrected using the formula:  $\text{K}_2\text{O}_{\text{corr}} = \text{molar} [m \times Al_2O_3 + m \times (CaO^* + Na_2O)] / (1 - m)$ , where  $m = K / (A + C^* + N + K)$  for protolith [56,57]. Alternatively, the influence of K-metasomatism can also be identified by the Al<sub>2</sub>O<sub>3</sub> – CaO\* + Na<sub>2</sub>O – K<sub>2</sub>O (A-CN-K) ternary diagram [58]. The K-corrected CIA value is expressed as  $\text{CIA}_{\text{corr}}$ .

#### 4. Results

All geochemical data for the Meiziwan section are given in the Supplementary Materials Table S1, and key geochemical data are shown in Figure 4. TOC and  $\text{Ba}_{\text{xs}}$  values generally increase upwards, ranging from 1.5 to 6.3 wt.% (mean 4.4 wt.%) and 984 ppm

to 23022 ppm (mean 3640 ppm), respectively;  $\delta^{13}\text{C}_{\text{org}}$  ranges from  $-35.41$  to  $-31.82\%$  (mean  $-33.07\%$ ); Al ranges from 4.61 to 7.71 wt.% (mean 6.66 wt.%);  $\text{Fe}_T$  ranges from 0.4 to 2.8 wt.% (mean 1.0 wt.%);  $\text{Fe}_{\text{HR}}/\text{Fe}_T$  ranges from 0.21 to 0.76 (mean 0.54);  $\text{Fe}_{\text{py}}/\text{Fe}_{\text{HR}}$  ranges from 0 to 0.48 (mean 0.07); Mo ranges from 17.4 to 188.2 ppm (mean 80.3 ppm);  $\text{Mo}_{\text{EF}}$  ranges from 28.5 to 262.9 (mean 121.8); U ranges from 19.3 to 41.4 ppm (mean 27.0 ppm);  $\text{U}_{\text{EF}}$  ranges from 8.5 to 19.3 (mean 13.3); Mo and U concentrations, as well as  $\text{Mo}_{\text{EF}}$  and  $\text{U}_{\text{EF}}$  values are more variable in the low part of the section, while generally remain constant in the upper part of the section. Mo/TOC ranges from 6 to 59 (mean 20); CIA and  $\text{CIA}_{\text{corr}}$  generally displays a decreasing trend upwards, ranging from 66.6 to 80.2 (mean 72.4) and 73.9 to 88.2 (mean 81.0), respectively.

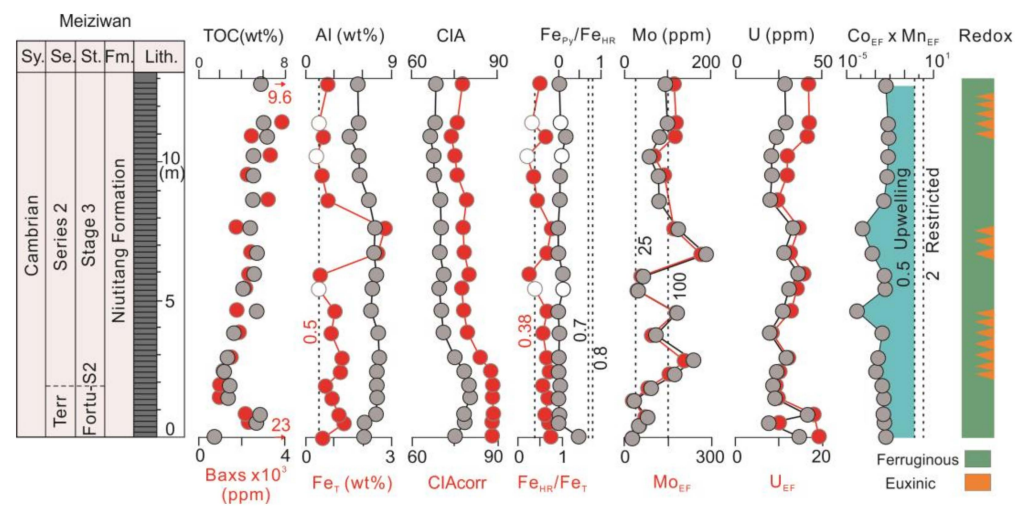


**Figure 4.** Chemostratigraphic profiles of key geochemical proxies and redox summary for the Meiziwan section. Gray circles correspond to the top axis and red circles correspond to the bottom axis. The vertical dashed lines represent key proxy threshold values (see text for discussion). The unfilled circles in  $\text{Fe}_T$ ,  $\text{Fe}_{\text{HR}}/\text{Fe}_T$ , and  $\text{Fe}_{\text{py}}/\text{Fe}_{\text{HR}}$  represent samples containing  $<0.5$  wt.%  $\text{Fe}_T$ . Note that two  $\text{Ba}_{\text{XS}}$  outliers at the top and bottom are not shown. Abbreviations: Sy. = System; Se. = Series; St. = Stage; Fm. = Formation; Lith. = Lithology.

## 5. Discussion

### 5.1. Evaluation of Redox Conditions

Sedimentary Fe speciation has been proven as a reliable proxy when investigating marine redox conditions [22,59–63]. Marine sediments deposited under anoxic water column generally yield  $\text{Fe}_{\text{HR}}/\text{Fe}_T > 0.38$ ; additionally, the ratio of  $\text{Fe}_{\text{py}}/\text{Fe}_{\text{HR}}$  can be applied to distinguish euxinic (anoxic and  $\text{H}_2\text{S}$ -enriched) conditions ( $\text{Fe}_{\text{py}}/\text{Fe}_{\text{HR}} > 0.8$ ) from ferruginous (anoxic and  $\text{Fe}^{2+}$ -enriched) conditions ( $\text{Fe}_{\text{py}}/\text{Fe}_{\text{HR}} < 0.7$ ) [62]. Due to the uncertainty of Fe speciation in samples containing a small amount of  $\text{Fe}_T$ , Fe speciation is only applied to samples with  $\text{Fe}_T$  values  $> 0.5$  wt.% [64].

Redox-sensitive trace elements (RSTEs) have been widely used for paleoredox reconstruction recently [42,65–68]. Seawater Mo dominantly comes from riverine delivery ( $\sim 90\%$ ), while hydrothermal processes contribute only 10% [69]. In oxic water column conditions, Mo is soluble and present as conservative molybdate ( $\text{MoO}_4^{2-}$ ). Meanwhile, in the presence of free  $\text{H}_2\text{S}$ ,  $\text{MoO}_4^{2-}$  is easily shifted to particle-reactive thiomolybdates ( $\text{MoO}_{4-x}\text{S}_x^{2-}$ ,  $x = 1-4$ ), and can be efficiently removed to the sediment via adsorption onto OM and formation of Fe-Mo-S compounds, resulting in the enrichment of Mo in sedimentary rocks [70,71]. As for seawater U, riverine delivery contributes the major input flux, while dust and submarine groundwater discharge provide minor input fluxes (Lau et al., 2019) [72]. U is present as soluble  $\text{U}^{6+}$  in oxic water column and can be transformed to insoluble  $\text{U}^{4+}$  around the  $\text{Fe}^{3+}$ - $\text{Fe}^{2+}$  redox boundary [71,73]. Compilation of modern marine RSTEs data indicates that Mo concentrations are commonly  $<25$  ppm for non-euxinic conditions, 25–100 ppm for perma-

nently Mo-depleted euxinic conditions or intermittently/seasonally euxinic conditions, and >100 ppm for permanently euxinic conditions [74].

At Meiziwan, samples with  $Fe_T > 0.5$  wt.% are characterized by moderate to high  $Fe_{HR}/Fe_T$  (0.25–0.76, mean 0.59) and consistently low  $Fe_{py}/Fe_{HR}$  (0.00–0.48, mean 0.07) (Figure 4), suggesting dominantly ferruginous conditions. However, high concentrations of Mo (17.4–188.2 ppm, mean 80.3 ppm), U (19.3–41.4 ppm, mean 27.0 ppm) and high  $Mo_{EF}$  (28.5–262.9, mean 121.8),  $U_{EF}$  (8.5–19.3, mean 13.3) values (Figure 4) indicate at least intermittently euxinic conditions during the Niutitang period. It has been proposed that low  $Fe_{py}/Fe_{HR}$  ratios are more reliable in recognizing conditions that are dominantly ferruginous, while elevated Mo–U concentrations are more sensitive/useful in distinguishing episodes of euxinia [42]. Therefore, these mixed redox signals at Meiziwan probably reflect fluctuating redox conditions during the deposition of the Niutitang Formation, and we thus infer that the Niutitang black shales were most likely deposited under dominantly ferruginous conditions with intermittently euxinic episodes. Similar Fe–Mo–U signal combinations for the Niutitang Formation and inferred redox conditions have also been documented in other sections from the upper Yangtze Platform (e.g., Jinsha, Weng'an) [42].

### 5.2. Marine Productivity

The proxy TOC has been broadly used as an indicator of primary productivity of surface water [7,13,18–20,75,76]. As the single largest constituent of organic matter, organic carbon represents the most direct indicator for primary productivity, although it commonly represents a small portion of fixed-carbon that is produced through photosynthesis and eventually reached the sediment–water interface [7,17,77]. On the other side, the TOC value of sediment is not just the result of primary productivity, but also preservation condition, sedimentation rate and dilution effect of organic carbon as well [9].

Excess barium (or biological Ba; i.e.,  $Ba_{xs}$ ) is also applied as a primary productivity indicator, as Ba enrichment is commonly associated with the development of microenvironments resulting from the decay process [17,19,20,77–80]. Nevertheless, it should be noted that Ba may be mobilized under the euxinic water column during early diagenesis, limiting its use as a primary productivity index [71]. As discussed in Section 5.1, the predominance of ferruginous water conditions (euxinia only appeared occasionally, i.e., episodes) during the OM accumulation would tone down the opposite effects of recycling of Ba out from sediments. On the other hand, increased seawater sulfate level during the E–C transition [81] would enable sufficient  $SO_4^{2-}$  to diffuse downward deeper into sediments, hence enhancing the preservation of barite (i.e., Ba) [82]. All these factors thus bolster the use of Ba as a primary productivity proxy. At Meiziwan, there is a good positive correlation between  $Ba_{xs}$  and TOC contents ( $R^2 = 0.55$ ; Figure 5), suggesting a strong production control on organic matter accumulation and indicating that both proxies can be utilized to estimate primary productivity at Meiziwan [17,20]. Similar  $Ba_{xs}$ –TOC signature and indication have also been documented in the Shuijingtuo Formation of the Luojiacun section, Hubei Province (the upper Yangtze Platform) [19]. Samples from high primary productivity areas of modern equatorial Pacific are generally characterized by high  $Ba_{xs}$  concentrations of ~1000–5000 ppm [83]. For the Meiziwan section, samples have high concentrations of  $Ba_{xs}$  ranging from 984 to 3829 ppm (except two outliers, see in Figure 5), with an average concentration of 2145 ppm. These values are generally within the range of modern equatorial Pacific high productivity areas, suggesting Ba enrichments in the study section are comparable to values from high primary productivity environments, and further enables the use of Ba as a primary productivity proxy. TOC contents range from 1.5 to 6.3 wt.% with an average of 4.4 wt.%, also indicating high productivity during the deposition of the Niutitang Formation.

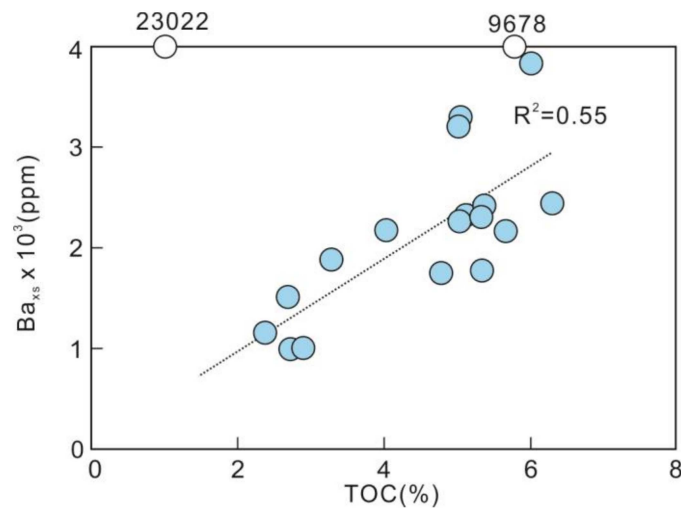


**Figure 5.** Crossplot of  $Ba_{xs}$  and TOC contents for the Meiziwan section. Note that the two samples which are considered as outliers (unfilled symbols) were not included in the correlation.

**5.3. Chemical Weathering of Source Area and Terrestrial Fluxes at Meiziwan**

The chemical index of alteration (CIA) has been widely applied to quantitatively reconstruct weathering intensity of source rocks [54,84–87]. Normally, CIA values lower than 70 indicate a low degree of chemical weathering in a cold and arid climate conditions, while CIA values higher than 80 present a high degree of chemical weathering under warm and wet climate conditions [54,85]. However, CIA could be affected by K-metasomatism during diagenesis, thus an  $Al_2O_3 - CaO^* + Na_2O - K_2O$  (i.e., A-CN-K) ternary diagram was used here to assess the possible influence of K-metasomatism [58] (Figure 6). Theoretically, the ideal trend of weathering of the source rock should be parallel to the A-CN sideline. The weathering trend of our samples here deviated from the ideal line, which is indicative of K-metasomatism of our samples [58].

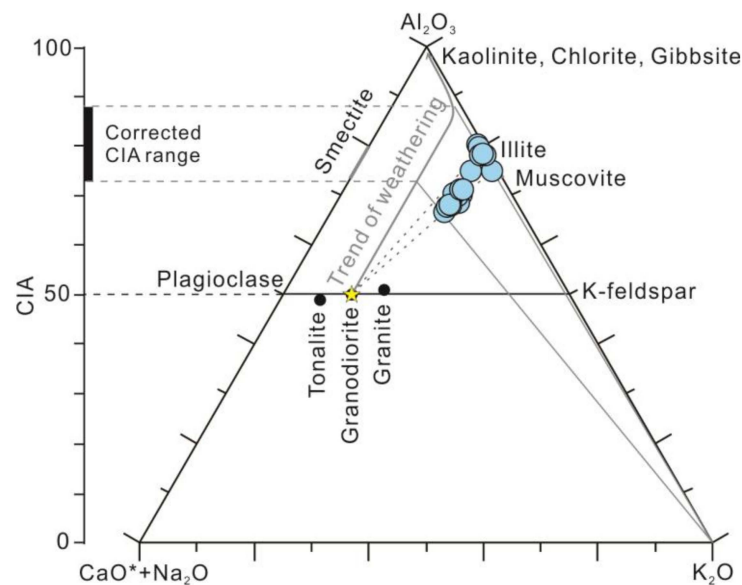


**Figure 6.** A-CN-K ternary diagram of the samples from the Meiziwan section. Tonalite, granodiorite, and granite data are from Condie [88]. CIA—Chemical Index of Alteration, A— $Al_2O_3$ , CN— $CaO^* + Na_2O$ , K— $K_2O$  (all in molar proportions),  $CaO^*$ —Ca incorporated in the silicate fraction of the sample, Pl—plagioclase, Kfs—K-feldspar, Sm—smectite, Ka—kaolinite, Chl—chlorite, Gi—gibbsite, Mu—muscovite.

In order to correct the influence of K-metasomatism, we conducted provenance composition analyses of the Meiziwan section. Crossplots of  $TiO_2$  vs. Zr are adopted here to

distinguish igneous rock types [84,85,87,89], with  $\text{TiO}_2/\text{Zr}$  ratios of  $<55$  for felsic rocks, 55–195 for intermediate rocks, and  $>195$  for mafic rocks [89]. Our Meiziwan samples are characterized by low  $\text{TiO}_2/\text{Zr}$  ratios (32–57, mean 41), suggesting their source rocks for the Niutitang black shales are mainly felsic (Figure 7A). The ternary diagram of La–Th–Sc also indicates that the source rock types are dominantly granodiorite (Figure 7B) [90]. Additional evidence for the source rock type also comes from the Th/Co vs. La/Sc diagram [91], suggesting predominantly silicic rocks of the source rock (Figure 7C). All together, the data exhibit such a granodiorite source rock for the Meiziwan section and consistent provenance composition. Therefore, corrections for K-metasomatism on CIA values were conducted based on a granodiorite source rock compositions (details are shown in Section 3).

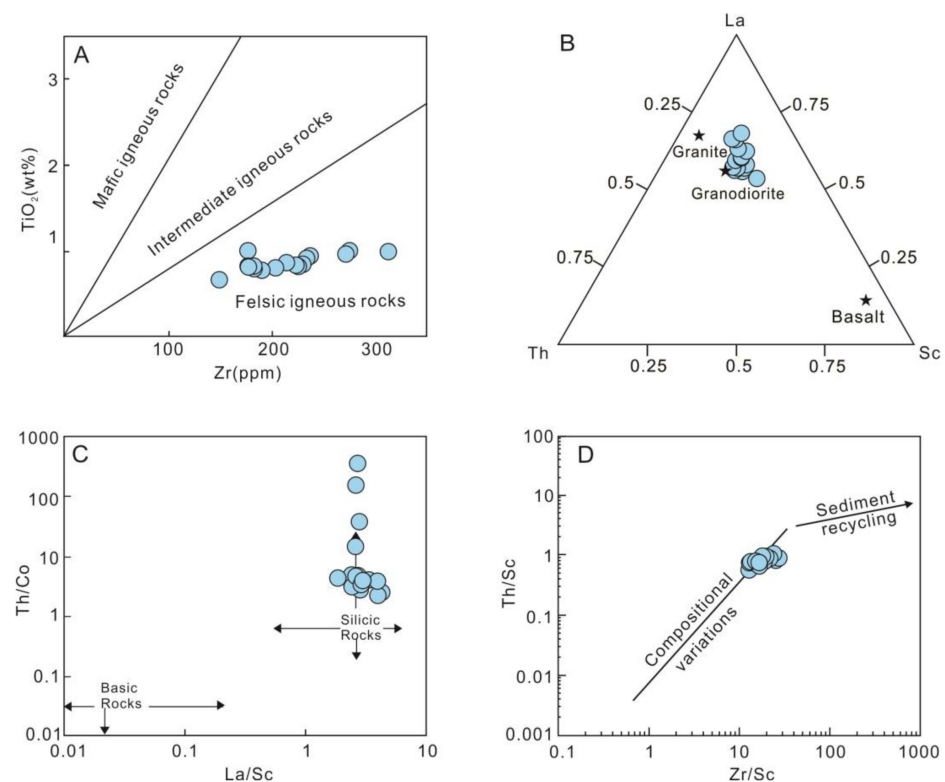


**Figure 7.** Discrimination diagrams illustrating sedimentary provenance and recycling effect. (A)  $\text{TiO}_2$  vs. Zr [89]. Samples from Niutitang Formation suggest that the source rocks were predominantly felsic. (B) La–Th–Sc ternary diagram [90]. Samples from Niutitang Formation are plot close to granodiorite. (C) Th/Co vs. La/Sc diagram [91]. Samples from Niutitang Formation are consistent with a silicic rocks source. (D) Th/Sc vs. Zr/Sc diagram [88]. Samples from Niutitang Formation plot in the area with no sediment recycling effect.

Additionally, sediment recycling could also exert a large effect on CIA values. Plot of Th/Sc vs. Zr/Sc ratios are adopted here to evaluate this effect [84,85,87,92]. McLennan et al. [92] suggested that first-cycle sediments commonly follow the compositional trend of source rocks, whereas recycled sediments show a tendency of substantial zircon increases. Our Meiziwan samples (Figure 7D) are consistent with the compositional variations trend of the parent rocks, and low Zr/Sc ratios (12.8 to 27.37, mean 18.16) exhibit here suggest that the effect of sediment recycling is very limited, thus enabling the CIA proxy to be applied as a chemical weathering indicator.

Chemical weathering may exert an effect on organic carbon accumulation via the adsorption of organic compounds onto clay minerals produced during chemical weathering, resulting in a weak positive correlation between CIA and TOC [93]. However,  $\text{CIA}_{\text{corr}}$  vs. TOC at Meiziwan generally exhibit a negative correlation, with the highest TOC content correspond to the lowest  $\text{CIA}_{\text{corr}}$  value (Figure 8), suggesting chemical weathering of parent

rocks was not an important factor controlling the organic matter accumulation at Meiziwan. However, the shift from high CIA values to low CIA values (note the decreasing trend upsection) might indicate a transition to cooler climate environment. Similar phenomena and indication have also been documented at Daotuo section, Guizhou Province, for the Ediacaran-Cambrian successions [87]. Terrigenous fluxes were another factor that could affect the accumulation of organic matter in sediments. Aluminum is generally immobile during diagenesis and originates overwhelmingly from detrital input [94], and was selected here to assess the terrigenous fluxes. Our sample exhibits low Al contents (mean 6.66%), indicating low terrigenous input. Additionally, the negative relationship between TOC and Al contents rule out the possibility that terrestrial organic matter controlled the sedimentary organic matter at Meiziwan and suggest that the decreased TOC contents was most likely a result of enhanced clastic dilution (Figure 9).

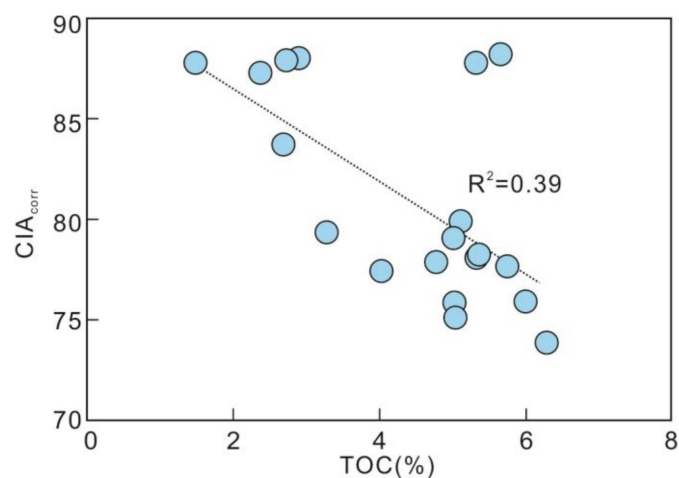


**Figure 8.** Crossplot of CIA<sub>corr</sub> vs. TOC for the Meiziwan sediments.

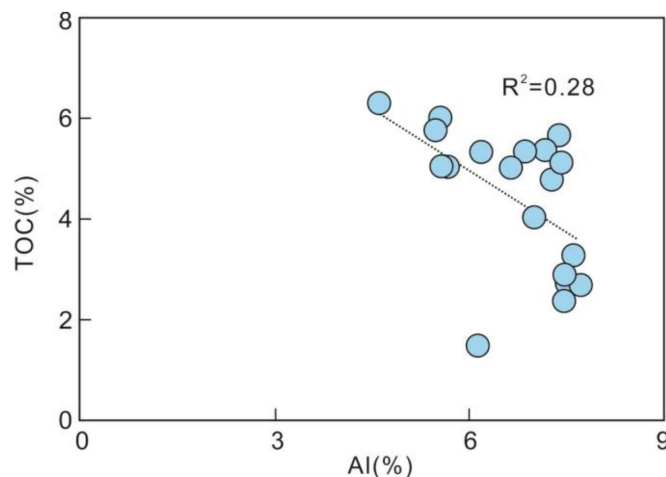


**Figure 9.** Crossplot of Al vs. TOC for the Meiziwan sediments.

#### 5.4. Upwelling and Watermass Restriction at Meiziwan

Previous studies have inferred strong upwelling event during the deposition of the organic-rich Niutitang black shales based on the geochemical cycling of C-P-Fe-Ba elements as well as the widespread occurrence of phosphorites and phosphate nodules at the basal part of the Niutitang Formation [20,21,23,24,36]. Here, we use the proxy of  $Co_{EF} \times Mn_{EF}$  in order to distinguish upwelling environments from other marine conditions [13,23,95,96]. In upwelling environments, supply of nutrients are primarily dominated by upwelling of deeper waters which is depleted in Co and Mn; while in restricted basins, supply of

nutrients are largely driven by riverine input that are enriched in Co and Mn [95]. Another process that results in the depletion of Mn (probably also the Co) in upwelling areas is the so called “conveyor belt” that transport Mn away to the open ocean [95]. Therefore, upwelling environments are characterized by remarkable depletion of Co and Mn concentrations, as well as the value of  $Co_{EF} \times Mn_{EF}$  below 0.5 [95]. Specifically, areas under the influence of persistent upwelling event (e.g., Peruvian Margin) yield much lower  $Co_{EF} \times Mn_{EF}$  values than those with only transient upwelling event influence (e.g., Gulf of California) [13,95]. At Meiziwan, samples are characterized by fairly low  $Co_{EF} \times Mn_{EF}$  values (<0.01), thus indicating strong upwelling event during the deposition of these organic-rich shales of the Niutitang Formation (Figure 10).

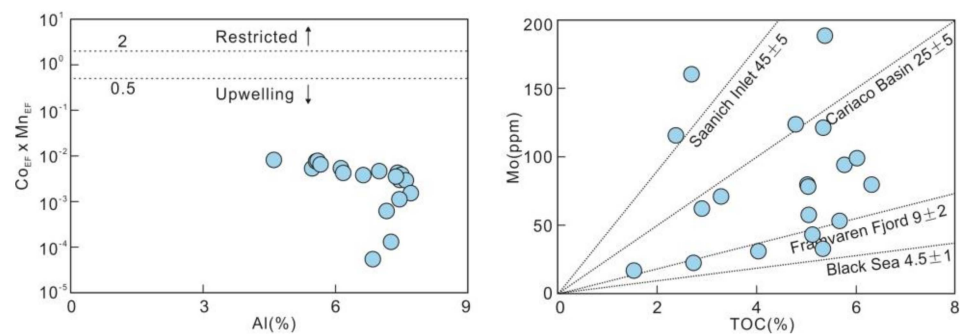


**Figure 10.** Crossplot of  $Co_{EF} \times Mn_{EF}$  vs. Al showing upwelling influence for the Meiziwan sediments, and the dashed lines are adopted from Sweere et al. [95]. Crossplot of TOC vs. Mo indicating generally good connection between Meiziwan and the open ocean, and the trend lines are modified from Algeo and Lyons [70].

The watermass restriction could be estimated using the proxy of Mo/TOC. Compilation of numerous Mo/TOC ratios of modern silled basins suggests that Mo/TOC could be applied to distinguish different levels of watermass restriction, with values of <15, ~15–35, and >35, indicating strong, moderate and weak restriction, respectively [70]. However, it should be noted that euxinic conditions were widespread during the early Cambrian, resulting in large amounts of Mo removal to the sediments and lower aqueous Mo and reduced Mo/TOC ratios [70]. Cheng et al. [97] proposed that low Mo/TOC values (1–22 ppm/wt.%) are representative of the early Cambrian global ocean, instead of restricted watermass. In the Meiziwan section, most samples (16 of 19) fall in the range within 6–26 ppm/wt.%, exhibiting a common phenomenon for Lower Cambrian strata and indicating weak to non-restricted watermass.

##### 5.5. Controls on Organic Matter Accumulation on the Early Cambrian Yangtze Platform

The grand transgression initiating at the very beginning of Cambrian is indicated by abrupt lithological transition from the Dengying shallow water dolostone to the Liuchapo deeper water bedded cherts [33,36,98]. This transgression would have enhanced upwelling events through increasing ocean overturn rates [99,100]. In addition, Yeasmin et al. [21] also proposed that the oceanic upwelling on the Yangtze Platform was further enhanced by the northeasterly trade winds and offshore current during the early Cambrian based on the paleolatitude position of the Yangtze Block [101,102]. Furthermore, the shift to a cooler climate environment (Figure 4, note the trend towards lower CIA values upsection) would lead to a rising of thermocline and nutricline [87]. These factors would greatly promote nutrient-rich deeper oceanic waters being upwelled into surface water, stimulating phytoplankton bloom and primary productivity in the surface water greatly and enhancing organic matter accumulation afterwards (Figure 4, note the increasing trend of TOC and  $Ba_{xs}$  values upsection) [21–23,103,104]. This process was likely aided by the concurrent hydrothermal addition that containing extraneous nutrients input (e.g., Ba, Ni, Cu, Zn) [18,20,32,33,105]. In addition, a low terrigenous fluxes at Meiziwan section (evidenced by low Al contents;

Figure 4) during upwelling process limited dilution effect of organic matter in the sediments. Collectively, these factors altogether leading to the widespread organic-rich black shales during the Niutitang period and phosphorites and phosphate nodules as well, especially on the shelf regions [20,23,24,36,106]. On the other hand, the anoxic conditions would result in more efficient P recycling, enhancing primary productivity in surface water [107,108]. Meanwhile, elevated accumulation of organic matter would promote subsequent bacterial sulfate reduction process, leading to the occurrence of episodes of euxinia and, thus, reconciling the redox conditions at Meiziwan, as well as at Jinsha sections [23,42].

## 6. Conclusions

Geochemical profiles of C isotopes, Fe speciation, major and trace elements, and CIA data were obtained for organic-rich black shales of the lower Cambrian Meiziwan section (South China), which was located in the upper slope area of the upper Yangtze Platform. Our results suggest a strong production control on organic matter accumulation and show that upwelling events exerted a fundamental control on the deposition of organic-rich Niutitang black shales at Meiziwan. The upwelling events bring nutrient-rich bottom waters into the surface water, thus greatly stimulating the phytoplankton bloom and primary productivity in the surface water and facilitating organic matter enrichment. On the other hand, the enhanced accumulation of organic matter could have accelerated subsequent bacterial sulfate reduction process, resulting in the dominantly ferruginous conditions with episodes of euxinia in the upper slope area and promoting preservation of large amounts of organic matter. In summary, our study emphasize the key role of oceanic upwelling on the marine primary productivity on the earliest Cambrian Yangtze Platform.

**Supplementary Materials:** The following supporting information can be downloaded at: <https://www.mdpi.com/article/10.3390/min13020260/s1>, Table S1: Key geochemical data discussed in the study for the Meiziwan Section.

**Author Contributions:** Conceptualization, G.Z. and D.C.; methodology, G.Z., D.C., Y.D. and T.H.; investigation, G.Z., D.C., Y.D. and T.H.; resources, G.Z., D.C., Y.D. and T.H.; data curation, G.Z. and T.H.; writing—original draft preparation, G.Z.; writing—review and editing, G.Z., Y.D. and T.H.; supervision, G.Z. and D.C.; project administration, D.C.; funding acquisition, D.C.. All authors have read and agreed to the published version of the manuscript.

**Funding:** This research was funded by the National Natural Science Foundation of China (91755210, 41472089).

**Data Availability Statement:** The data are presented in the Supplementary Materials.

**Acknowledgments:** Xiqiang Zhou is thanked for the assistance during the preparation of field trip. We thank Linlin Cui, Dingshuai Xue, Yanhong Liu, Li Su and Hongyu Zhang for their laboratory assistance.

**Conflicts of Interest:** The authors declare no conflict of interest.

## References

1. Amthor, J.E.; Grotzinger, J.P.; Schröder, S.; Bowring, S.A.; Ramezani, J.; Martin, M.W.; Matter, A. Extinction of Cloudina and Namacalathus at the Precambrian-Cambrian boundary in Oman. *Geology* **2003**, *31*, 431–434. [[CrossRef](#)]
2. Li, Z.X.; Bogdanova, S.V.; Collins, A.S.; Davidson, A.; De Waele, B.; Ernst, R.E.; Fitzsimons, I.C.W.; Fuck, R.A.; Gladkochub, D.P.; Jacobs, J.; et al. Assembly, configuration, and break-up history of Rodinia: A synthesis. *Precambrian Res.* **2008**, *160*, 179–210. [[CrossRef](#)]
3. Knoll, A.H.; Carroll, S.B. Early animal evolution: Emerging views from comparative biology and geology. *Science* **1999**, *284*, 2129–2137. [[CrossRef](#)] [[PubMed](#)]
4. Condie, K.C.; Des Marais, D.J.; Abbott, D. Precambrian superplumes and supercontinents: A record in black shales, carbon isotopes, and paleoclimates? *Precambrian Res.* **2001**, *106*, 239–260. [[CrossRef](#)]
5. Zou, C.; Zhu, R.; Chen, Z.-Q.; Ogg, J.G.; Wu, S.; Dong, D.; Qiu, Z.; Wang, Y.; Wang, L.; Lin, S.; et al. Organic-matter-rich shales of China. *Earth Sci. Rev.* **2019**, *189*, 51–78. [[CrossRef](#)]
6. Arthur, M.A.; Sageman, B.B. Marine Black Shales: Depositional Mechanisms and Environments of Ancient Deposits. *Annu. Rev. Earth Planet. Sci.* **1994**, *22*, 499–551. [[CrossRef](#)]

7. Pedersen, T.F.; Calvert, S.E. Anoxia vs. productivity: What controls the formation of organic- carbon-rich sediments and sedimentary rocks? *Aapg Bull.* **1990**, *74*, 454–466.
8. Sageman, B.B.; Murphy, A.E.; Werne, J.P.; Ver Straeten, C.A.; Hollander, D.J.; Lyons, T.W. A tale of shales: The relative roles of production, decomposition, and dilution in the accumulation of organic-rich strata, Middle–Upper Devonian, Appalachian basin. *Chem. Geol.* **2003**, *195*, 229–273. [[CrossRef](#)]
9. Tyson, R.V. The “productivity versus preservation” controversy: Cause, flaws, and resolution. In *Deposition of Organiccarbon-rich Sediments: Models, Mechanisms, and Consequences*; Harris, N.B., Ed.; Society for Sedimentary Geology, Special Publication: Tulsa, OK, USA, 2005; pp. 17–33.
10. Caplan, M.L.; Bustin, R.M. Palaeoceanographic controls on geochemical characteristics of organic-rich Exshaw mudrocks: Role of enhanced primary production. *Org. Geochem.* **1998**, *30*, 161–188. [[CrossRef](#)]
11. Wei, H.; Chen, D.; Wang, J.; Yu, H.; Tucker, M.E. Organic accumulation in the lower Chihsia Formation (Middle Permian) of South China: Constraints from pyrite morphology and multiple geochemical proxies. *Palaeogeogr. Palaeoclimatol. Palaeoecol.* **2012**, *353*, 73–86. [[CrossRef](#)]
12. Kumar, S.P.; Ramaiah, N.; Gauns, M.; Sarma, V.V.S.S.; Madhupratap, M. Physical forcing of biological productivity in the Northern Arabian Sea during the Northeast Monsoon. *Deep Sea Res. Part II* **2001**, *48*, 1115–1126. [[CrossRef](#)]
13. Zhang, B.; Yao, S.; Wignall, P.B.; Hu, W.; Ding, H.; Liu, B.; Ren, Y. Widespread coastal upwelling along the Eastern Paleo-Tethys Margin (South China) during the Middle Permian (Guadalupian): Implications for organic matter accumulation. *Mar. Pet. Geol.* **2018**, *97*, 113–126. [[CrossRef](#)]
14. Demaison, G.J.; Moore, G.T. Anoxic environments and oil source bed genesis. *Org. Geochem.* **1980**, *2*, 9–31. [[CrossRef](#)]
15. Jenkyns, H.C. Geochemistry of oceanic anoxic events. *Geochem. Geophys. Geosyst.* **2010**, *11*, 427–428. [[CrossRef](#)]
16. Calvert, S.E.; Karlin, R.E.; Toolin, L.J.; Donahue, D.J.; Southon, J.R.; Vogel, J.S. Low organic carbon accumulation rates in Black Sea sediments. *Nature* **1991**, *350*, 692–695. [[CrossRef](#)]
17. Schoepfer, S.D.; Shen, J.; Wei, H.Y.; Tyson, R.V.; Ingall, E.; Algeo, T.J. Total organic carbon, organic phosphorus, and biogenic barium fluxes as proxies for paleomarine productivity. *Earth-Sci. Rev.* **2015**, *149*, 23–52. [[CrossRef](#)]
18. Gao, P.; Liu, G.D.; Jia, C.Z.; Young, A.; Wang, Z.C.; Wang, T.S.; Zhang, P.W.; Wang, D.P. Redox variations and organic matter accumulation on the Yangtze carbonate platform during Late Ediacaran–Early Cambrian: Constraints from petrology and geochemistry. *Palaeogeogr. Palaeoclimatol. Palaeoecol.* **2016**, *450*, 91–110. [[CrossRef](#)]
19. Liu, K.; Feng, Q.; Shen, J.; Khan, M.; Planavsky, N.J. Increased productivity as a primary driver of marine anoxia in the Lower Cambrian. *Palaeogeogr. Palaeoclimatol. Palaeoecol.* **2018**, *491*, 1–9. [[CrossRef](#)]
20. Wu, Y.; Tian, H.; Gong, D.; Li, T.; Zhou, Q. Paleo-environmental variation and its control on organic matter enrichment of black shales from shallow shelf to slope regions on the Upper Yangtze Platform during Cambrian Stage 3. *Palaeogeogr. Palaeoclimatol. Palaeoecol.* **2020**, *545*, 109653. [[CrossRef](#)]
21. Yeasmin, R.; Chen, D.Z.; Fu, Y.; Wang, J.G.; Guo, Z.H.; Guo, C. Climatic-oceanic forcing on the organic accumulation across the shelf during the Early Cambrian (Age 2 through 3) in the mid-upper Yangtze Block, NE Guizhou, South China. *J. Asian Earth Sci.* **2017**, *134*, 365–386. [[CrossRef](#)]
22. Huang, T.Y.; Chen, D.Z.; Fu, Y.; Yeasmin, R.; Guo, C. Development and evolution of a euxinic wedge on the ferruginous outer shelf of the early Cambrian Yangtze sea. *Chem. Geol.* **2019**, *524*, 259–271. [[CrossRef](#)]
23. Jin, C.S.; Li, C.; Algeo, T.J.; Wu, S.Y.; Cheng, M.; Zhang, Z.H.; Shi, W. Controls on organic matter accumulation on the early-Cambrian western Yangtze Platform, South China. *Mar. Pet. Geol.* **2020**, *111*, 75–87. [[CrossRef](#)]
24. Gao, P.; He, Z.; Li, S.; Lash, G.G.; Li, B.; Huang, B.; Yan, D. Volcanic and hydrothermal activities recorded in phosphate nodules from the Lower Cambrian Niutitang Formation black shales in South China. *Palaeogeogr. Palaeoclimatol. Palaeoecol.* **2018**, *505*, 381–397. [[CrossRef](#)]
25. Liu, Z.H.; Zhuang, X.G.; Teng, G.E.; Xie, X.M.; Yin, L.M.; Bian, L.Z.; Feng, Q.L.; Algeo, T.J. The lower Cambrian Niutitang Formation at Yangtiao (Guizhou, SW China): Organic matter enrichment, source rock potential, and hydrothermal influences. *J. Pet. Geol.* **2015**, *38*, 411–432. [[CrossRef](#)]
26. Zhang, K.; Song, Y.; Jiang, S.; Jiang, Z.; Jia, C.; Huang, Y.; Wen, M.; Liu, W.; Xie, X.; Liu, T.; et al. Mechanism analysis of organic matter enrichment in different sedimentary backgrounds: A case study of the Lower Cambrian and the Upper Ordovician-Lower Silurian, in Yangtze region. *Mar. Pet. Geol.* **2019**, *99*, 488–497. [[CrossRef](#)]
27. Zhang, Y.Y.; He, Z.L.; Jiang, S.; Gao, B.; Liu, Z.B.; Han, B.; Wang, H. Marine redox stratification during the early Cambrian (ca. 529–509 Ma) and its control on the development of organic-rich shales in Yangtze Platform. *Geochem. Geophys. Geosyst.* **2017**, *18*, 2354–2369. [[CrossRef](#)]
28. Charvet, J. The Neoproterozoic–Early Paleozoic tectonic evolution of the South China Block: An overview. *J. Asian Earth Sci.* **2013**, *74*, 198–209. [[CrossRef](#)]
29. Wang, J.; Li, Z.X. History of Neoproterozoic rift basins in South China: Implications for Rodinia break-up. *Precambrian Res.* **2003**, *122*, 141–158. [[CrossRef](#)]
30. Ding, Y.; Chen, D.Z.; Zhou, X.Q.; Guo, C.; Huang, T.Y.; Zhang, G.J. Tectono-depositional pattern and evolution of the middle Yangtze Platform (South China) during the late Ediacaran. *Precambrian Res.* **2019**, *333*, 105426. [[CrossRef](#)]
31. Korsch, R.J.; Mai, H.Z.; Sun, Z.C.; Gorter, J.D. The Sichuan basin, southwest China: A late proterozoic (Sinian) petroleum province. *Precambrian Res.* **1991**, *54*, 45–63. [[CrossRef](#)]

32. Chen, D.Z.; Wang, J.G.; Qing, H.R.; Yan, D.T.; Li, R.W. Hydrothermal venting activities in the Early Cambrian, South China: Petrological, geochronological and stable isotopic constraints. *Chem. Geol.* **2009**, *258*, 168–181. [[CrossRef](#)]
33. Wang, J.G.; Chen, D.Z.; Wang, D.; Yan, D.T.; Zhou, X.Q.; Wang, Q.C. Petrology and geochemistry of chert on the marginal zone of Yangtze Platform, western Hunan, South China, during the Ediacaran–Cambrian transition. *Sedimentology* **2012**, *59*, 809–829. [[CrossRef](#)]
34. Liu, J.H.; Yang, P.; Wang, Z.J.; Zhuo, J.W.; Du, Q.D. Paleo-weathering crust at the top of Sinian Dengying Formation in northern Guizhou and its petroleum exploration significance. *Geol. China* **2012**, *39*, 931–938.
35. Ding, Y.; Li, Z.; Liu, S.; Song, J.; Zhou, X.; Sun, W.; Zhang, X.; Li, S.; Ran, B.; Peng, H.; et al. Sequence stratigraphy and tectono-depositional evolution of a late Ediacaran epeiric platform in the upper Yangtze area, South China. *Precambrian Res.* **2021**, *354*, 106077. [[CrossRef](#)]
36. Chen, D.Z.; Zhou, X.Q.; Fu, Y.; Wang, J.G.; Yan, D.T. New U–Pb zircon ages of the Ediacaran–Cambrian boundary strata in South China. *Terra Nova* **2015**, *27*, 62–68. [[CrossRef](#)]
37. Compston, W.; Zhang, Z.C.; Cooper, J.A.; Ma, G.; Jenkins, R.J. Further shrimp geochronology on the early cambrian of south china. *Am. J. Sci.* **2008**, *308*, 399–420. [[CrossRef](#)]
38. Okada, Y.; Sawaki, Y.; Komiya, T.; Hirata, T.; Takahata, N.; Sano, Y.; Han, J.; Maruyama, S. New chronological constraints for Cryogenian to Cambrian rocks in the Three Gorges, Weng’an and Chengjiang areas, South China. *Gondwana Res.* **2014**, *25*, 1027–1044. [[CrossRef](#)]
39. Wang, X.Q.; Shi, X.Y.; Jiang, G.Q.; Zhang, W.H. New U–Pb age from the basal Niutitang Formation in South China: Implications for diachronous development and condensation of stratigraphic units across the Yangtze platform at the Ediacaran–Cambrian transition. *J. Asian Earth Sci.* **2012**, *48*, 1–8. [[CrossRef](#)]
40. McKerrow, W.S.; Scotese, C.R.; Brasier, M.D. Early Cambrian continental reconstructions. *J. Geol. Soc.* **1992**, *149*, 599–606. [[CrossRef](#)]
41. Jin, C.S. Spatiotemporal Variations of Ocean Redox Conditions and Its Co-Evolution with Early Animals during the Early Cambrian, South China. Ph.D. Dissertation, China University of Geosciences, Wuhan, China, 2017.
42. Jin, C.S.; Li, C.; Algeo, T.J.; Planavsky, N.J.; Cui, H.; Yang, X.L.; Zhao, Y.L.; Zhang, X.L.; Xie, S.C. A highly redox-heterogeneous ocean in South China during the early Cambrian (~529–514 Ma): Implications for biota-environment co-evolution. *Earth Planet. Sci. Lett.* **2016**, *441*, 38–51. [[CrossRef](#)]
43. Chang, H.J.; Chu, X.L.; Feng, L.J.; Huang, J.; Chen, Y.L. Marine redox stratification on the earliest Cambrian (ca. 542–529 Ma) Yangtze Platform. *Palaeogeogr. Palaeoclimatol. Palaeoecol.* **2018**, *504*, 75–85. [[CrossRef](#)]
44. Goldberg, T.; Strauss, H.; Guo, Q.J.; Liu, C.Q. Reconstructing marine redox conditions for the Early Cambrian Yangtze Platform: Evidence from biogenic sulphur and organic carbon isotopes. *Palaeogeogr. Palaeoclimatol. Palaeoecol.* **2007**, *254*, 175–193. [[CrossRef](#)]
45. Shen, Y.; Schidlowski, M. New C isotope stratigraphy from southwest China: Implications for the placement of the Precambrian–Cambrian boundary on the Yangtze Platform and global correlations. *Geology* **2000**, *28*, 623–626. [[CrossRef](#)]
46. Wang, J.G.; Chen, D.Z.; Yan, D.T.; Wei, H.Y.; Xiang, L. Evolution from an anoxic to oxidic deep ocean during the Ediacaran–Cambrian transition and implications for bioradiation. *Chem. Geol.* **2012**, *306*, 129–138. [[CrossRef](#)]
47. Hayes, J.M.; Strauss, H.; Kaufman, A.J. The abundance of <sup>13</sup>C in marine organic matter and isotopic fractionation in the global biogeochemical cycle of carbon during the past 800 Ma. *Chem. Geol.* **1999**, *161*, 103–125. [[CrossRef](#)]
48. Kump, L.R.; Arthur, M.A. Interpreting carbon-isotope excursions: Carbonates and organic matter. *Chem. Geol.* **1999**, *161*, 181–198. [[CrossRef](#)]
49. Guo, Q.; Strauss, H.; Zhu, M.; Zhang, J.; Yang, X.; Lu, M.; Zhao, F. High resolution organic carbon isotope stratigraphy from a slope to basinal setting on the Yangtze Platform, South China: Implications for the Ediacaran–Cambrian transition. *Precambrian Res.* **2013**, *225*, 209–217. [[CrossRef](#)]
50. Wang, X.Q.; Shi, X.Y.; Zhao, X.K.; Tang, D.J. Increase of seawater Mo inventory and ocean oxygenation during the early Cambrian. *Palaeogeogr. Palaeoclimatol. Palaeoecol.* **2015**, *440*, 621–631. [[CrossRef](#)]
51. Taylor, S.R.; McLennan, S.M. *The Continental Crust: Its Composition and Evolution*; BlackwellScientificPublications: Oxford, UK, 1985.
52. Poulton, S.W.; Canfield, D.E. Development of a sequential extraction procedure for iron: Implications for iron partitioning in continentally derived particulates. *Chem. Geol.* **2005**, *214*, 209–221. [[CrossRef](#)]
53. Canfield, D.E.; Raiswell, R.; Westrich, J.T.; Reaves, C.M.; Berner, R.A. The use of chromium reduction in the analysis of reduced inorganic sulfur in sediments and shales. *Chem. Geol.* **1986**, *54*, 149–155. [[CrossRef](#)]
54. Nesbitt, H.W.; Young, G.M. Early Proterozoic climates and plate motions inferred from major element chemistry of lutites. *Nature* **1982**, *299*, 715–717. [[CrossRef](#)]
55. McLennan, S.M. Weathering and global denudation. *J. Geol.* **1993**, *101*, 295–303. [[CrossRef](#)]
56. Panahi, A.; Young, G.M.; Rainbird, R.H. Behavior of major and trace elements (including REE) during Paleoproterozoic pedogenesis and diagenetic alteration of an Archean granite near Ville Marie, Quebec, Canada. *Geochim. Cosmochim. Acta* **2000**, *64*, 2199–2220. [[CrossRef](#)]
57. Rieu, R.; Allen, P.A.; Plötze, M.; Pettko, T. Climatic cycles during a Neoproterozoic “snowball” glacial epoch. *Geology* **2007**, *35*, 299–302. [[CrossRef](#)]
58. Fedo, C.M.; Nesbitt, H.W.; Young, G.M. Unraveling the effects of potassium metasomatism in sedimentary rocks and paleosols, with implications for paleoweathering conditions and provenance. *Geology* **1995**, *23*, 921–924. [[CrossRef](#)]

59. Canfield, D.E.; Poulton, S.W.; Knoll, A.H.; Narbonne, G.M.; Ross, G.; Goldberg, T.; Strauss, H. Ferruginous conditions dominated later neoproterozoic deep-water chemistry. *Science* **2008**, *321*, 949–952. [[CrossRef](#)]
60. Li, C.; Love, G.D.; Lyons, T.W.; Fike, D.A.; Sessions, A.L.; Chu, X.L. A stratified redox model for the Ediacaran ocean. *Science* **2010**, *328*, 80–83. [[CrossRef](#)]
61. Poulton, S.W. The Iron Speciation Paleoredox Proxy. In *Elements in Geochemical Tracers in Earth System Science*; Lyons, T., Turchyn, A., Reinhard, C., Eds.; Cambridge University Press: Cambridge, UK, 2021.
62. Poulton, S.W.; Canfield, D.E. Ferruginous conditions: A dominant feature of the ocean through Earth's history. *Elements* **2011**, *7*, 107–112. [[CrossRef](#)]
63. Zhang, Z.H.; Li, C.; Cheng, M.; Algeo, T.J.; Jin, C.S.; Tang, F.; Huang, J.H. Evidence for Highly Complex Redox Conditions and Strong Water-Column Stratification in an Early Cambrian Continental-Margin Sea. *Geochem. Geophys. Geosyst.* **2018**, *19*, 2397–2410. [[CrossRef](#)]
64. Clarkson, M.O.; Poulton, S.W.; Guilbaud, R.; Wood, R.A. Assessing the utility of Fe/Al and Fe-speciation to record water column redox conditions in carbonate-rich sediments. *Chem. Geol.* **2014**, *382*, 111–122. [[CrossRef](#)]
65. Bennett, W.W.; Canfield, D.E. Redox-sensitive trace metals as paleoredox proxies: A review and analysis of data from modern sediments. *Earth Sci. Rev.* **2020**, *204*, 103175. [[CrossRef](#)]
66. Sahoo, S.K.; Planavsky, N.J.; Kendall, B.; Wang, X.Q.; Shi, X.Y.; Scott, C.; Anbar, A.D.; Lyons, T.W.; Jiang, G.Q. Ocean oxygenation in the wake of the Marinoan glaciation. *Nature* **2012**, *489*, 546–549. [[CrossRef](#)] [[PubMed](#)]
67. Wu, Y.; Tian, H.; Li, J.; Li, T.; Ji, S. Reconstruction of oceanic redox structures during the Ediacaran-Cambrian transition in the Yangtze Block of South China: Implications from Mo isotopes and trace elements. *Precambrian Res.* **2021**, *359*, 106181. [[CrossRef](#)]
68. Zhao, X.K.; Wang, X.Q.; Shi, X.Y.; Tang, D.J.; Shi, Q. Stepwise oxygenation of early Cambrian ocean controls early metazoan diversification. *Palaeogeogr. Palaeoclimatol. Palaeoecol.* **2018**, *504*, 86–103. [[CrossRef](#)]
69. McManus, J.; Nägler, T.F.; Siebert, C.; Wheat, C.G.; Hammond, D.E. Oceanic molybdenum isotope fractionation: Diagenesis and hydrothermal ridge-flank alteration. *Geochem. Geophys. Geosyst.* **2002**, *3*, 1–9. [[CrossRef](#)]
70. Algeo, T.J.; Lyons, T.W. Mo-total organic carbon covariation in modern anoxic marine environments: Implications for analysis of paleoredox and paleohydrographic conditions. *Paleoceanography* **2006**, *21*, 10–16. [[CrossRef](#)]
71. Tribouillard, N.; Algeo, T.J.; Lyons, T.; Riboulleau, A. Trace metals as paleoredox and paleoproductivity proxies: An update. *Chem. Geol.* **2006**, *232*, 12–32. [[CrossRef](#)]
72. Lau, K.V.; Romaniello, S.J.; Zhang, F. The Uranium Isotope Paleoredox Proxy. In *Elements in Geochemical Tracers in Earth System Science*; Lyons, T., Turchyn, A., Reinhard, C., Eds.; Cambridge University Press: Cambridge, UK, 2019.
73. Algeo, T.J.; Tribouillard, N. Environmental analysis of paleoceanographic systems based on molybdenum–uranium covariation. *Chem. Geol.* **2009**, *268*, 211–225. [[CrossRef](#)]
74. Scott, C.; Lyons, T.W. Contrasting molybdenum cycling and isotopic properties in euxinic versus non-euxinic sediments and sedimentary rocks: Refining the paleoproxies. *Chem. Geol.* **2012**, *324*, 19–27. [[CrossRef](#)]
75. Ge, X.; Chen, D.; Zhang, G.; Huang, T.; Liu, M.; El-Shafey, M. Marine redox evolution and organic accumulation in an intrashelf basin, NE Sichuan Basin during the Late Permian. *Mar. Pet. Geol.* **2022**, *140*, 105633. [[CrossRef](#)]
76. Liao, Z.; Hu, W.; Cao, J.; Wang, X.; Fu, X. Oceanic anoxia through the late Permian Changhsingian Stage in the Lower Yangtze region, South China: Evidence from sulfur isotopes and trace elements. *Chem. Geol.* **2020**, *532*, 119371. [[CrossRef](#)]
77. Canfield, D.E. Factors influencing organic carbon preservation in marine sediments. *Chem. Geol.* **1994**, *114*, 315–329. [[CrossRef](#)]
78. Dymond, J.; Suess, E.; Lyle, M. Barium in deep-sea sediment: A geochemical proxy for paleoproductivity. *Paleoceanography* **1992**, *7*, 163–181. [[CrossRef](#)]
79. Paytan, A.; Griffith, E.M. Marine barite: Recorder of variations in ocean export productivity. *Deep Sea Res. Part II* **2007**, *54*, 687–705. [[CrossRef](#)]
80. Zhai, L.; Wan, S.; Tada, R.; Zhao, D.; Shi, X.; Yin, X.; Tan, Y.; Li, A. Links between iron supply from Asian dust and marine productivity in the Japan Sea since four million years ago. *Geol. Mag.* **2019**, *157*, 818–828. [[CrossRef](#)]
81. Algeo, T.J.; Luo, G.M.; Song, H.Y.; Lyons, T.W.; Canfield, D.E. Reconstruction of secular variation in seawater sulfate concentrations. *Biogeosciences* **2015**, *12*, 2131–2151. [[CrossRef](#)]
82. Zhou, X.; Chen, D.; Dong, S.; Zhang, Y.; Guo, Z.; Wei, H.; Yu, H. Diagenetic barite deposits in the Yurtus Formation in Tarim Basin, NW China: Implications for barium and sulfur cycling in the earliest Cambrian. *Precambrian Res.* **2015**, *263*, 79–87. [[CrossRef](#)]
83. Murray, R.; Leinen, M. Chemical transport to the seafloor of the equatorial Pacific Ocean across a latitudinal transect at 135° W: Tracking sedimentary major, trace, and rare earth element fluxes at the Equator and the Intertropical Convergence Zone. *Geochim. Cosmochim. Acta* **1993**, *57*, 4141–4163. [[CrossRef](#)]
84. Li, C.; Zhang, Z.; Jin, C.; Cheng, M.; Wang, H.; Huang, J.; Algeo, T.J. Spatiotemporal evolution and causes of marine euxinia in the early Cambrian Nanhua Basin (South China). *Palaeogeogr. Palaeoclimatol. Palaeoecol.* **2020**, *546*, 109676. [[CrossRef](#)]
85. Yan, D.; Chen, D.; Wang, Z.; Li, J.; Yang, X.; Zhang, B. Climatic and oceanic controlled deposition of Late Ordovician-Early Silurian black shales on the North Yangtze platform, South China. *Mar. Pet. Geol.* **2019**, *110*, 112–121. [[CrossRef](#)]
86. Yan, D.T.; Chen, D.Z.; Wang, Q.C.; Wang, J.G. Large-scale climatic fluctuations in the latest Ordovician on the Yangtze block, south China. *Geology* **2010**, *38*, 599–602. [[CrossRef](#)]

87. Zhai, L.N.; Wu, C.D.; Ye, Y.T.; Zhang, S.C.; Wang, Y.Z. Fluctuations in chemical weathering on the Yangtze Block during the Ediacaran–Cambrian transition: Implications for paleoclimatic conditions and the marine carbon cycle. *Palaeogeogr. Palaeoclimatol. Palaeoecol.* **2018**, *490*, 280–292. [[CrossRef](#)]
88. Condie, K.C. Chemical composition and evolution of the upper continental crust: Contrasting results from surface samples and shales. *Chem. Geol.* **1993**, *104*, 1–37. [[CrossRef](#)]
89. Hayashi, K.I.; Fujisawa, H.; Holland, H.D.; Ohmoto, H. Geochemistry of ~1.9 Ga sedimentary rocks from northeastern Labrador, Canada. *Geochim. Cosmochim. Acta* **1997**, *61*, 4115–4137. [[CrossRef](#)] [[PubMed](#)]
90. Cullers, R.L.; Podkovyrov, V.N. Geochemistry of the Mesoproterozoic Lakhanda shales in southeastern Yakutia, Russia: Implications for mineralogical and provenance control, and recycling. *Precambrian Res.* **2000**, *104*, 77–93. [[CrossRef](#)]
91. Cullers, R.L. Implications of elemental concentrations for provenance, redox conditions, and metamorphic studies of shales and limestones near Pueblo, CO, USA. *Chem. Geol.* **2002**, *191*, 305–327. [[CrossRef](#)]
92. McLennan, S.M.; Hemming, S.R.; Mcdaniel, D.K.; Hanson, G.N. Geochemical approaches to sedimentation, provenance, and tectonics. In *Processes Controlling the Composition of Clastic Sediments*; Johnsson, M.J., Basu, A., Eds.; Geological Society of America, Special Paper; Geological Society of America: Boulder, CO, USA, 1993; pp. 21–40.
93. Tosca, N.J.; Johnston, D.T.; Mushegian, A.A.; Rothman, D.H.; Summons, R.E.; Knoll, A.H. Clay mineralogy, organic carbon burial, and redox evolution in Proterozoic oceans. *Geochim. Cosmochim. Acta* **2010**, *74*, 1579–1592. [[CrossRef](#)]
94. Algeo, T.J.; Maynard, J.B. Trace-element behavior and redox facies in core shales of Upper Pennsylvanian Kansas-type cyclothems. *Chem. Geol.* **2004**, *206*, 289–318. [[CrossRef](#)]
95. Sweere, T.; van den Boorn, S.; Dickson, A.J.; Reichart, G.-J. Definition of new trace-metal proxies for the controls on organic matter enrichment in marine sediments based on Mn, Co, Mo and Cd concentrations. *Chem. Geol.* **2016**, *441*, 235–245. [[CrossRef](#)]
96. Yang, S.; Hu, W.; Wang, X. Mechanism and implications of upwelling from the Late Ordovician to early Silurian in the Yangtze region, South China. *Chem. Geol.* **2021**, *565*, 30. [[CrossRef](#)]
97. Cheng, M.; Li, C.; Zhou, L.; Algeo, T.J.; Zhang, F.; Romaniello, S.; Jin, C.-S.; Lei, L.-D.; Feng, L.-J.; Jiang, S.-Y. Marine Mo biogeochemistry in the context of dynamically euxinic mid-depth waters: A case study of the lower Cambrian Niutitang shales, South China. *Geochim. Cosmochim. Acta* **2016**, *183*, 79–93. [[CrossRef](#)]
98. Haq, B.U.; Schutter, S.R. A chronology of Paleozoic sea-level changes. *Science* **2008**, *322*, 64–68. [[CrossRef](#)]
99. Arthur, M.A.; Schlanger, S.O.; Jenkyns, H.C. *The Cenomanian-Turonian Oceanic Anoxic Event, II. Palaeoceanographic Controls on Organic-Matter Production and Preservation*; Special Publications; Geological Society: London, UK, 1987; Volume 26, pp. 401–420.
100. Arthur, M.A.; Sageman, B.B. Sea-level control on source-rock development: Perspectives from the Holocene Black Sea, the mid-Cretaceous Western Interior Basin of North America, and the Late Devonian Appalachian Basin. In *The Deposition of Organic-Carbon-Rich Sediments: Models, Mechanisms, and Consequences*; Harris, N.B., Ed.; Society for Sedimentary Geology: Tulsa, OK, USA, 2005; pp. 35–59.
101. Scotese, C.; Boucot, A.; McKerrow, W. Gondwanan palaeogeography and palaeoclimatology. *J. Afr. Earth Sci.* **1999**, *28*, 99–114. [[CrossRef](#)]
102. Golonka, J. Phanerozoic paleoenvironment and paleolithofacies maps. *Early Paleozoic. Geol./Akad. Górniczo-Hut. Im. Stanisława Staszica W Krakowie* **2007**, *35*, 589–654.
103. Coale, K.H.; Fitzwater, S.E.; Gordon, R.M.; Johnson, K.S.; Barber, R.T. Control of community growth and export production by upwelled iron in the equatorial Pacific Ocean. *Nature* **1996**, *379*, 621–624. [[CrossRef](#)]
104. Resing, J.A.; Sedwick, P.N.; German, C.R.; Jenkins, W.J.; Moffett, J.W.; Sohst, B.M.; Tagliabue, A. Basin-scale transport of hydrothermal dissolved metals across the South Pacific Ocean. *Nature* **2015**, *523*, 200–203. [[CrossRef](#)]
105. Och, L.M.; Shields-Zhou, G.A.; Poulton, S.W.; Manning, C.; Thirlwall, M.F.; Li, D.; Chen, X.; Ling, H.F.; Osborn, T.; Cremonese, L. Redox changes in Early Cambrian black shales at Xiaotan section, Yunnan Province, South China. *Precambrian Res.* **2013**, *225*, 166–189. [[CrossRef](#)]
106. Ye, Y.; Wang, H.; Wang, X.; Zhai, L.; Wu, C.; Zhang, S. Elemental geochemistry of lower Cambrian phosphate nodules in Guizhou Province, South China: An integrated study by LA-ICP-MS mapping and solution ICP-MS. *Palaeogeogr. Palaeoclimatol. Palaeoecol.* **2020**, *538*. [[CrossRef](#)]
107. Wignall, P.B. *Black Shales*; Oxford University Press: New York, NY, USA, 1994.
108. Algeo, T.J.; Ingall, E. Sedimentary Corg:P ratios, paleocean ventilation, and Phanerozoic atmospheric pO<sub>2</sub>. *Palaeogeogr. Palaeoclimatol. Palaeoecol.* **2007**, *256*, 130–155. [[CrossRef](#)]

**Disclaimer/Publisher’s Note:** The statements, opinions and data contained in all publications are solely those of the individual author(s) and contributor(s) and not of MDPI and/or the editor(s). MDPI and/or the editor(s) disclaim responsibility for any injury to people or property resulting from any ideas, methods, instructions or products referred to in the content.